Cavity formation at metal–water interfaces

Thorben Eggert ; Nicolas G. Hörmann ; Karsten Reuter

Check for updates

View Online

Export Citation

CrossMark

Cavity formation at metal–water interfaces

View Online   Export Citation   CrossMark

Thorben Eggert,[1,2] (iD) Nicolas G. Hörmann,[1,a)] (iD) and Karsten Reuter[1] (iD)

AFFILIATIONS

[1] Fritz-Haber-Institut der Max-Planck-Gesellschaft, Faradayweg 4-6, 14195 Berlin, Germany

[2] Chair of Theoretical Chemistry and Catalysis Research Center, Technische Universität München, Lichtenbergstr. 4, 85748 Garching, Germany

[a)]Author to whom correspondence should be addressed: hoermann@fhi.mpg.de

ABSTRACT

The free energy cost of forming a cavity in a solvent is a fundamental concept in rationalizing the solvation of molecules and ions. A detailed understanding of the factors governing cavity formation in bulk solutions has *inter alia* enabled the formulation of models that account for this contribution in coarse-grained implicit solvation methods. Here, we employ classical molecular dynamics simulations and multistate Bennett acceptance ratio free energy sampling to systematically study cavity formation at a wide range of metal–water interfaces. We demonstrate that the obtained size- and position-dependence of cavitation energies can be fully rationalized by a geometric Gibbs model, which considers that the creation of the metal–cavity interface necessarily involves the removal of interfacial solvent. This so-called competitive adsorption effect introduces a substrate dependence to the interfacial cavity formation energy that is missed in existing bulk cavitation models. Using expressions from scaled particle theory, this substrate dependence is quantitatively reproduced by the Gibbs model through simple linear relations with the adsorption energy of a single water molecule. Besides providing a better general understanding of interfacial solvation, this paves the way for the derivation and efficient parametrization of more accurate interface-aware implicit solvation models needed for reliable high-throughput calculations toward improved electrocatalysts.

I. INTRODUCTION

Atomistically resolved simulations of liquids are particularly challenging due to the simultaneous presence of dynamic disorder and significant chemical interactions, such as H-bonding networks in aqueous solutions.[1–4] In particular, when it comes to solvation, there is, therefore, a long-standing tradition to replace explicit dynamical simulations with a statistically relevant number of solvent molecules through computationally more efficient coarse-grained simulations. The corresponding implicit solvation approaches then embed the finite, atomically resolved solute (molecule or ion) into a solvent region that, in the simplest case, is merely described as a dielectric continuum.[5,6] Not least from the angle of such implicit solvation models, cavity formation and concomitant cavity formation energies thus emerge as fundamental concepts in the general understanding of solvation. The latter energies denote the free energy cost of creating an excluded volume V_{cav} in the solvent that can then be occupied by the solute.

At a constant pressure, the cavitation free energy arises simply from the created internal interface between the solvent at the outside and vacuum at the inside of the cavity. It, therefore, scales naturally with the surface area of the cavity A_{cav}, with a liquid–cavity (LC) surface tension γ_{LC} as a proportionality factor,

$$F_{cav,\,bulk} = \gamma_{LC} A_{cav}. \tag{1}$$

For large enough cavities, this proportionality factor is the macroscopic liquid–vapor (LV) surface tension, $\gamma_{LC} \to \gamma_{LV}$ for $A_{cav} \to \infty$.[7–9] For smaller cavities, γ_{LC} is generally size-dependent. Within scaled particle theory (SPT), this size dependency can be derived rigorously for spherical cavities and expressed as a polynomial expansion in the cavity radius.[8,10,11] For small cavities, the thus approximately linear scaling of γ_{LC} with radius leads then overall to an approximate cubic scaling of $F_{cav,\,bulk}$ with radius, i.e., $F_{cav,\,bulk} \propto V_{cav}$ for $V_{cav} \to 0$.[7–9,12–15] As a result, it is not surprising that appropriately parametrized, effective continuum solvation models that use area and/or volume scaling to approximate $F_{cav,\,bulk}$[6,11,16,17] succeed in accurately reproducing experimental solvation energies of different species in aqueous[16,17] and non-aqueous[18,19] bulk solvent environments.

More recently, according models have been applied to study the stability of adsorbates at extended solid–liquid interfaces (SLIs), for which an accurate account of solvation effects is generally critical to reach the predictive accuracy necessary to develop, for example, improved electrocatalysts.[20–23] Unfortunately, however, the present bulk continuum models fail to reach this desired accuracy in the description of solvation at such interfaces.[20–24] One evident source of error is that these models are agnostic to competitive adsorption.[20,23,25,26] The latter describes the necessity to remove specifically bound solvent molecules from the surface to create space for the adsorbate. This is more difficult at strongly binding surfaces, and cavity formation should thus depend on the interaction strength between substrate and solvent.[24] Instead, the existing bulk parametrizations only consider the scaling with the overall cavity area and/or volume.

To quantify the energetic contribution of competitive adsorption and derive simple models for cavity formation at SLIs, we here employ free energy sampling methods for cavity formation at various metal–water interfaces using classical molecular dynamics (MD) simulations. By screening different sizes and distances of the cavity to the substrate, we obtain effective interface tensions for each SLI. We find that these correlate with the adsorption energy of an individual water molecule on a substrate, in agreement with the concept of competitive adsorption. Cast into a simple geometric Gibbs model, which accounts for the introduced and removed interfaces, these results provide the basis for the efficient parameterization of an interface-aware general cavity formation model. They also rationalize why competitive adsorption effects are, in some cases, less important than expected and where their account in atomistic SLI simulations will be critical.

II. METHODS

Our systematic MD simulations employ the SPC model (CVFF) for water[27] and classical metal–water potentials (12-6 Lennard-Jones) by Heinz and co-workers[28] to investigate eight different Me(111)–water SLIs (Me = Pt, Ni, Pd, Cu, Au, Ag, Al, and Pb) that cover a wide range of interaction strengths and thus competitive adsorption effects. The atomic structures were managed with the atomic simulation environment (ASE),[29] and the initial water slabs were created with Packmol.[30] The simulation cell contains a four-layer metal(111) slab with a (12×12) surface unit cell. The two lowest layers were fixed to their initial positions. A 25 Å thick water film above one side of the slab is followed by 20 Å wide vacuum on both sides. The simulations were performed with Large-scale Atomic/Molecular Massively Parallel Simulator (LAMMPS)[31] in a canonical ensemble (NVT) at 300 K, which yields cavity formation energies without pressure contributions since the water volume can freely readjust upon the creation of the cavity. The lattice constants and the number of water molecules for each system are reported in Table S1 of the supplementary material.

Cavities were modeled as soft spheres and interacted only with the oxygen atoms of water via a Weeks–Chandler–Andersen potential,[32]

$$U(r) = \begin{cases} 4\varepsilon \times \left[\left(\frac{\sigma}{r} \right)^{12} - \left(\frac{\sigma}{r} \right)^{6} \right] + \varepsilon, & r \leq 2^{1/6}\sigma, \\ 0, & r > 2^{1/6}\sigma, \end{cases} \quad (2)$$

which is a shifted and truncated Lennard-Jones potential; cf. Fig. S5 of the supplementary material.

It approaches zero smoothly at the cutoff $r_{\text{cut}} = 2^{1/6}\sigma$. The corresponding radius of a hard sphere was obtained through a Boltzmann factor criterion as $U(r = r_{\text{cav}}) = k_{\text{B}}T$.[33] We set $r_{\text{cav}} = r_{\text{cut}} - 0.5$Å for the different runs. Seven equally spaced cavity sizes r_{cav} between 2.5 and 5.5 Å were investigated in this study, and the lateral position of the cavity center was fixed to be above a top site. The z-coordinate of the cavity center was varied between $z_{\text{top}} - r_{\text{cut}}$ and $z_{\text{top}} + r_{\text{cut}} + 10$Å, where z_{top} is the position of the uppermost metal layer. Within this range, independent NVT-MDs runs were performed at every 0.25 Å at 300 K. The first 100 ps was used to equilibrate the system, and further 200 ps was used for data production. Atomic positions were saved every 1 ps. Ultimately, the free energy differences between all runs of one metal–water interface were calculated via MBAR as implemented in pymbar,[34]

$$\hat{f}_i = -\ln \sum_{j=1}^{K} \sum_{n=1}^{N_j} \frac{\exp\left[-u_i(x_{jn}) \right]}{\sum_{k=1}^{K} N_k \exp\left[\hat{f}_k - u_k(x_{jn}) \right]}, \quad (3)$$

where K denotes the thermodynamic states, N_j denote the uncorrelated equilibrium samples, u is the reduced potential, x denotes the atomic positions, and the index i is the state of interest. The equation is solved self-consistently for the dimensionless free energy $\hat{f}_i$, and then, all states are referenced to the initial state to obtain the free energy difference. This requires the calculation of the reduced (dimensionless) energy of all trajectories for one system with all possible cavity sizes and positions.

III. RESULTS AND DISCUSSION

A. Size dependence of cavitation energies at metal–water interfaces

Previous studies on the cavity formation energy on metal–water interfaces relied on particle insertion to access the spatially resolved free energy.[35,36] However, this approach is limited by the probability of finding cavities in an MD simulation, which becomes increasingly unlikely for larger ones. To drive the system to create larger cavities, they need to be explicitly included in the MD, and their respective free energy is calculated using free energy integration methods.[15] In this regard, our approach is similar to the work of Godawat and co-workers, who investigated the cavity formation free energy at self-assembled monolayers for large cavities (up to ∼10 Å).[37]

Exemplary cavity formation free energies $F_{\text{cav}}^{\text{MBAR}}$ for Pt(111) as a function of distance and cavity radius are plotted in Fig. 1(c). The results obtained for all other surfaces follow an analogous pattern; see below and Fig. S1 of the supplementary material. At most negative z_{cav}, the cavity is still completely inside the metal surface and $F_{\text{cav}}^{\text{MBAR}}$ is correspondingly zero.

We do not include any interaction between the metal and the cavity, since the focus of this work is to understand exclusively the free energy cost of creating a cavity, aka free space, within the solvent. In this regard, our approach is similar to the cavitation free energy costs in implicit solvation models, which have no repulsive interaction between the cavity and the substrate.[38] In order to understand how repulsive interactions between the substrate and a solute within the cavity would modify the overall free energy cost,
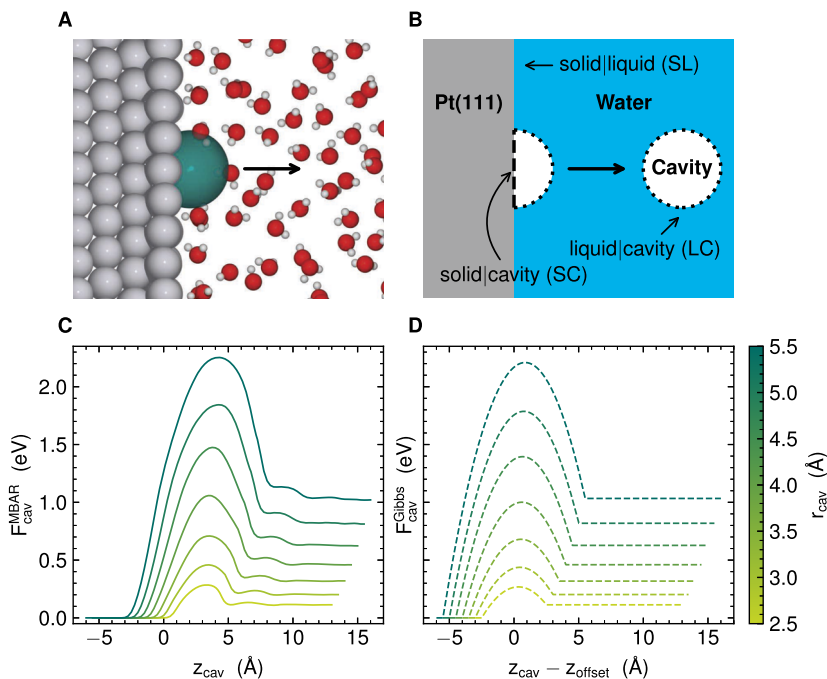
FIG. 1. Cavity formation at a Pt(111)–water interface. (a) Snapshot from an MD simulation with an explicit cavity cap emerging from the metal surface. (b) Continuum Gibbs model considering a sharp interface between the metal substrate and the solvent. The cavity creates new interfaces of the two subsystems with vacuum inside the cavity. (c) MD-simulated cavity formation free energy F_{cav}^{MBAR} as a function of distance of the cavity center to the Pt(111) surface z_{cav}. Results are shown for different cavity radii from 2.5 to 5.5 Å. (d) Corresponding cavity formation free energy F_{cav}^{Gibbs} from the Gibbs model fitted to the MD data. Note that the fitting procedure includes a z-shifting (z_{offset}) to align the curves in (c) and (d) (see the text).

we reevaluated the free energy calculations by adding a repulsive metal–cavity interaction identical to the water–cavity interaction (cf. Fig. S2 of the supplementary material), which leads to a sharp increase in F_{cav} for $z_{cav} < r_{cav}$, but the profiles remain unchanged for $z_{cav} > r_{cav}$.

With increasing z_{cav}, the cavity formation free energy then rises to an initial peak that is followed by a smaller peak or shoulder before it reaches a constant plateau value. Since all investigated metal surfaces in this study show perfect wetting ($W_{ad} > 2\gamma_{lv}$) and are hydrophilic,[28] this overall pattern can be rationalized qualitatively in a straightforward way by the additional cost to remove water from the substrate. With the cavity cap emerging from the metal surface at increasing z_{cav}, more and more water molecules are displaced from the interface to the bulk liquid. This leads to an increase in F_{cav}^{MBAR} up to a maximum, beyond which it reduces toward the bulk water level, where the favorable substrate–water interface has been reestablished. Obviously, both the initial peak and the plateau value thus also scale with the size of the cavity.

As explained in Fig. 1(b), we can cast this qualitative understanding into a simple geometric Gibbs model[39,40] that considers the sum of infinitely sharp continuum interfaces introduced by the cavity times their effective interface tensions,

$$F_{cav}^{Gibbs} = \gamma_{SC} \cdot A_{SC} + \gamma_{LC} \cdot A_{LC} - \gamma_{SL} \cdot A_{SC}$$
$$= \tilde{\gamma}^{Me} \cdot A_{SC} + \gamma_{LC} \cdot A_{LC}, \quad (4)$$

where A_{SC} is the contact area of the spherical cavity with the metallic surface and A_{LC} is the surface area of the cavity that is accessible to the solvent [cf. dashed and dotted lines in Fig. 1(b), respectively]. γ_{SC}, γ_{LC}, and γ_{SL} are the effective interface tensions for the different interfaces—solid–cavity (SC), liquid–cavity (LC), and solid–liquid (SL), respectively. $\tilde{\gamma}^{Me} = (\gamma_{SC} - \gamma_{SL})$ thus introduces competitive adsorption by accounting for the substrate-dependent differential cost of removing water from the metal contact area instead of creating an equally sized internal water–vacuum interface as considered in bulk solvation models.

As already mentioned initially, previous studies have clarified that for small cavities, a purely geometric Gibbs model with size-independent interface tensions fails in describing cavity formation in the case of bulk solvation.[7–9,12–15] We correspondingly fit Eq. (4) separately to the MD data obtained for each cavity radius, i.e., $\tilde{\gamma}^{Me} = \tilde{\gamma}^{Me}(r_{cav})$ and $\gamma_{LC} = \gamma_{LC}(r_{cav})$. The areas A_{SC} and A_{LC} are entirely determined by geometric considerations and are given by the cavity radius r_{cav}, the cavity position z_{cav}, and one offset fit parameter $z_{offset}^{Me}(r_{cav})$, which accounts for the shift between the position of the topmost metal layer atoms in the MD simulations and the idealized position of the SLI in the continuum model. $\gamma_{LC}(r_{cav})$ is assumed to be independent of the metal surface, consistent with a substrate-independent cavitation energy in bulk water. It is important to note here that making interface energies in Eq. (4) size-dependent allows us to capture any functional dependence on r_{cav}, including from common correction terms, such as the line tension. Figure 1(d)

shows F_{cav}^{Gibbs} obtained from the fit for Pt(111). It compares almost perfectly with the simulated F_{cav}^{MBAR} shown in Fig. 1(c), except for the second peak/shoulder. This feature is probably caused by the second water layer, which is not accounted for in the present Gibbs model and thus absent in F_{cav}^{Gibbs}. Previous studies on Au(100)[36,41] and Pt(100)/Pt(111)[35] reported a reduced cavity formation between the first and second water layers for small cavities. In addition, the study by Serva and co-workers reported that with increasing size, this position becomes unfavorable because the gap between the layers fits only small cavities.[36] Our results show the same behavior for the small cavities ($r_{cav} \leq 3$ Å), for which the profile in Fig. 1(b) shows a minimum between the two peaks caused by the water layers. For larger cavities, this becomes a shoulder and the cavity is destabilized compared to the bulk. A comparison of the heights of the two peaks clarifies that the cavity formation energy at the interface is dominated by the first water layer, which justifies the omission of second water layer effects in our energy model. It should be kept in mind, though, that the contribution of the second water layer can be ~0.15 eV for larger cavities.

Figure 2 shows the cavity-size dependence of the parameters $\gamma_{LC}(r_{cav})$ and $\tilde{\gamma}^{Me}(r_{cav})$ for Me = Pt. The results obtained for all other surfaces are listed in Table S2 of the supplementary material. Both interface tensions increase with cavity size. The roughly linear scaling for $r_{cav} \lesssim 4$ Å will lead to a cavity formation energy that scales proportional to the cavity volume, as often also included in continuum solvation models.[38,42,43] The saturation of $\gamma_{LC}(r_{cav})$ and $\tilde{\gamma}^{Pt}(r_{cav})$ slowly setting in for the larger r_{cav} values, in turn, indicates the approach to the area-scaling F_{cav} of an infinitely large cavity. The absolute values of $\gamma_{LC}(r_{cav})$ are in almost perfect quantitative agreement with those determined in earlier bulk cavity formation studies by Hummer et al.,[13] Floris et al.,[14] and Grigor'ev et al.[9]; cf. Figure 2(b). We attribute the small differences at larger cavities to differences in the employed water potential. The SPC model[44] employed by Hummer et al. and us (CVFF)[27] is known to underestimate the surface tension of liquid water[45] as compared to the TIP4P model[46] employed by Floris et al. and Grigor'ev et al.

We can accurately interpolate the similar and smooth size dependencies of $\tilde{\gamma}^{Me}(r_{cav})$ and $\gamma_{LC}(r_{cav})$ with the following expressions:

$$\tilde{\gamma}^{Me}(r_{cav}) = k_0^{Me}/r_{cav}^2 + k_1^{Me}/r_{cav} + \tilde{\gamma}_\infty^{Me},$$
$$\gamma_{LC}(r_{cav}) = k_0^{water}/r_{cav}^2 + k_1^{water}/r_{cav} + \gamma_{LV}, \tag{5}$$

where $\tilde{\gamma}_\infty^{Me}$ is the difference of the macroscopic solid–vapor and SL interface tensions and γ_{LV} is the afore-introduced macroscopic surface tension of liquid water. The coefficients k_0^{water}, k_1^{water} (and analogously k_0^{Me}, k_1^{Me}) relate to the coefficients of the polynomial expansion in r_{cav} for the cavity formation free energy on the basis of SPT as performed by Pierotti.[11] Mapping this expansion in r_{cav} back onto surface areas (r_{cav}^2) then naturally yields Eq. (5). The next higher order term that is proportional to the cavity volume was shown to be negligible at atmospheric pressures[8] and is apparently also not required for the data in Fig. 2. Within SPT, the coefficient k_1 is negative—consistent with the observations here—and related to the density of the liquid and the curvature of the cavity.[11,47] The other coefficient k_0 emerges from the atomistic dimension of the cavity and is absent in macroscopic thermodynamic descriptions.[8] Taking published $\tilde{\gamma}_\infty^{Me}$ for the employed interatomic potentials[28] and γ_{LV} from independent own simulations, we fit the coefficients k_0^{Me}, k_1^{Me} and k_0^{water}, k_1^{water} to obtain the accurate interpolations shown in Fig. 2 for Pt(111) and in Fig. S1 of the supplementary material for the other metals. The fitted coefficients for all interfaces are listed in Table S3 of the supplementary material. This accuracy, together with the overall similar size variations in $\tilde{\gamma}^{Me}(r_{cav})$ and $\gamma_{LC}(r_{cav})$, suggests that SPT considerations apply as well for the free energy cost of creating the two-dimensional cavity contact area at an SLI.

Furthermore, we performed additional free energy calculations for Pt(111) with a chain of cavities to test the applicability of Eq. (4). The chain consists of three stacked cavities, where the lowest cavity is centered in the interfacial water layer. We compared this setup with results for a single cavity placed at the same position. For a fixed total excluded volume, the two setups create different amounts of the areas A_{LC} and A_{SC}. Since the chain creates less A_{SC}, its cavity formation free energy is for all investigated excluded volumes lower than an equivalent single cavity at the interface, even though its total surface area is greater. Applying Eq. (4) and taking the coefficients from Table S2 of the supplementary material for both setups yields results in good agreement with the free energy calculations. These findings underline the possibility of separating interfacial cavity formation into two components, which depend on the solvent ($\gamma_{LC} \times A_{LC}$) and the substrate–solvent interface ($\tilde{\gamma}^{Me} \times A_{SC}$).

B. Variation with substrate

Figure 3(a) shows the MD-simulation results for the cavity formation free energy for Ni(111), Au(111), and Pb(111) and for a cavity radius of 5.5 Å. The corresponding data for the other metal surfaces and cavity sizes are provided in Fig. S1 of the supplementary material. All F_{cav}^{MBAR} collapse for $z_{cav} > 11$ Å. At these large distances from the surface, the cavity is fully immersed in the water and we consistently recover the substrate-independent bulk cavity formation free energy value. In contrast, a strong substrate dependence results for the prominent first peak where the cavity cap emerges from the surface—and to a lesser degree also for the small second peak/shoulder attributed to the second water layer. Not surprisingly from the perspective of competitive adsorption, this substrate dependence correlates with the binding strength of the substrate.
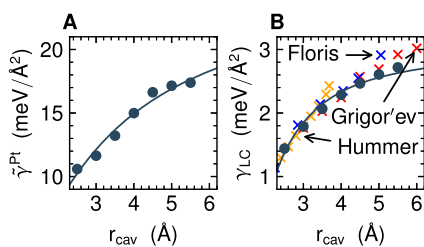

FIG. 2. Fitted parameters of the Gibbs model for the Pt(111)–water SLI as a function of cavity radius r_{cav}. (a) Effective interface tension $\tilde{\gamma}^{Pt}$ as extracted from the MD simulations (circles) and fit according to Eq. (5) (solid line). (b) Same for the effective surface tension for bulk water γ_{LC} (circles and solid line). The standard deviation is smaller than the size of the marker. The crosses show the reference data from bulk simulations of Floris et al. (blue),[14] Hummer et al. (orange),[13] and Grigor'ev et al. (red).[9]
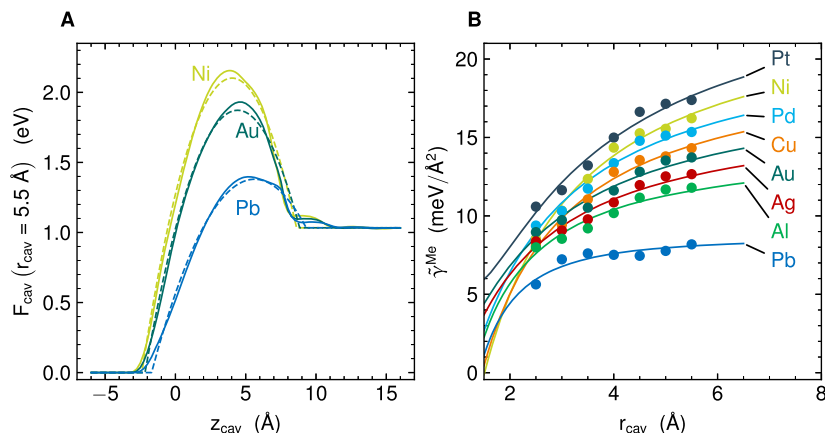
FIG. 3. Substrate dependence of the cavity formation free energy. (a) MD-simulated cavity formation free energy F_{cav}^{MBAR} (solid lines) and fitted Gibbs model F_{cav}^{Gibbs} (dashed lines) as a function of distance z_{cav} above Ni(111), Au(111), and Pb(111). Shown are the data for a fixed cavity radius of $r_{cav} = 5.5$ Å. (b) Fitted effective interface tension $\tilde{\gamma}^{Me}$ of the continuum Gibbs model as in Fig. 2(a), now for all eight metal surfaces.

It is much less favorable to form the cavity at the strongly binding Ni(111) surface as compared to Pb(111), and the ordering over the eight metals for the formation cost follows the one, for example, expected from the macroscopic work of adhesion of water at these surfaces: Pt > Ni > Pd > Cu > Au > Ag > Al > Pb.[28]

As apparent from Fig. 3(a) and Fig. S1 of the supplementary material, excellent fits to the MD data are also achieved for the other metals and cavity sizes, which then allows us to conveniently discuss the variations over substrates and cavity size on the basis of the $\tilde{\gamma}^{Me}$ interface tension that contributes the competitive adsorption related part to the overall cavity formation free energy. The corresponding data summarized in Fig. 3(b) reveal a size dependence for all metals that is analogous to the one discussed for Pt(111) before. All $\tilde{\gamma}^{Me}$ become smaller for smaller cavities. Intriguingly, they do so with different slopes though. For the strongest binding surfaces with the largest interface tension, the drop of $\tilde{\gamma}^{Me}$ toward smaller r_{cav} is also strongest. Expressed in the parameters of the SPT equation (5), the coefficient k_1^{Me} is thus always negative and more negative for the stronger interacting substrates. This makes perfect sense as denser liquids generally exhibit more negative k_1 coefficients.[8] All here

considered surfaces are wetting, which induces a water density peak directly at the SLI; cf. Fig. S4 of the supplementary material. This density peak is stronger for stronger interacting substrates, which, in turn, leads to more negative k_1^{Me} coefficients.

This understanding suggests that k_1^{Me} should also correlate with the adsorption energy of a single water molecule $E_{ads}^{H_2O}$, as the latter is a simple descriptor for the interaction strength at the SLI. The same correlation with $E_{ads}^{H_2O}$ should also hold for the $\tilde{\gamma}_\infty^{Me}$ parameter in Eq. (5), as this difference of the macroscopic solid–vapor and SL interface tensions trivially relates to the work of adhesion at the SLI for which the adsorption energy of a single water molecule is again a suitable descriptor.[48] In fact, we had already seen above that $\tilde{\gamma}^{Me}(r_{cav})$ for the larger cavity radius of 5.5 Å in Fig. 3(b) does follow the ordering expected from the work of adhesion. Figure 4 confirms this expected linear correlation and demonstrates that it also extends to the third parameter k_0^{Me} of the SPT equation (5). Expecting that these simple correlations equally hold for other inter-action potentials, for example, from first-principles calculations, suggests then a computationally highly efficient approach to param-eterize an interface-aware cavity formation free energy model for
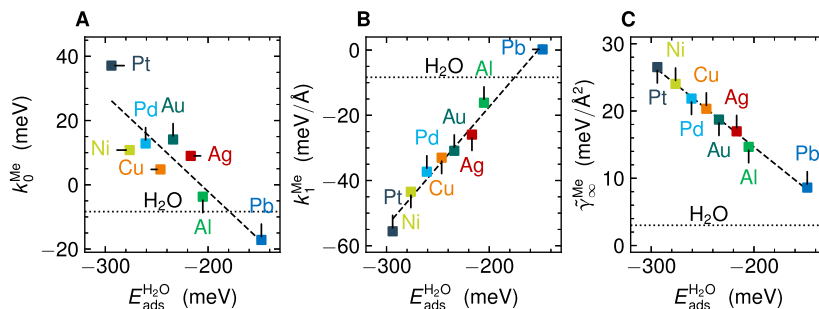

FIG. 4. Simple descriptor for the parameter determination of the Gibbs model. Correlation of all three parameters of the SPT equation (5) for the interface tension $\tilde{\gamma}^{Me}$ with the adsorption energy of a single water molecule $E_{ads}^{H_2O}$: (a) k_0^{Me}, (b) k_1^{Me}, and (c) $\tilde{\gamma}_\infty^{Me}$.
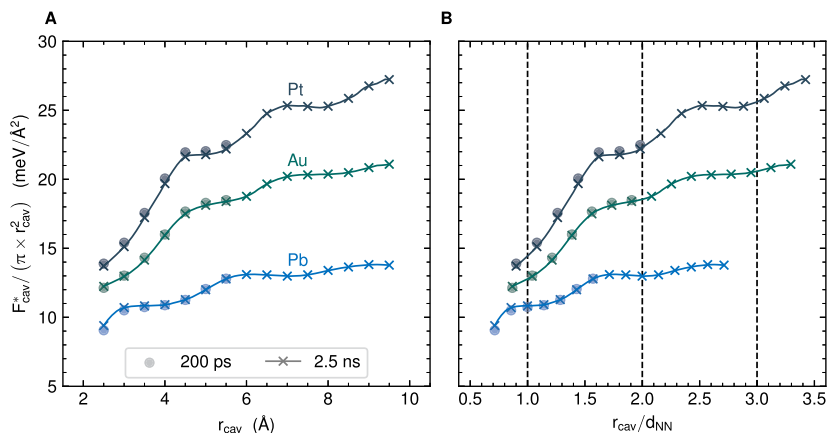
FIG. 5. Comparison of the area-normalized free energy of formation $F_{cav}^*/(\pi r_{cav}^2)$ of cavities positioned in the center of the density peak of the first water layer (Pt, Au: z_{cav} = 2.75 Å; Pb: z_{cav} = 3.00 Å) using MD runs of 200 ps and 2.5 ns. The results are plotted against the (a) absolute size of the cavity and (b) the size of the cavity relative to the nearest-neighbor distance d_{NN} with a solid line serving as a guide to the eye. The results demonstrate that convergence is already obtained from 200 ps MD sampling and that the oscillation frequency scales with the lattice of the underlying substrate. Further studies (see the text and supplementary material) confirm that they originate from the sequential exclusion of water adsorption on different adsorption sites.

substrates from all across the periodic system and any surface orientation. In this case, it would be sufficient to simulate ~3 cavity sizes for only two different materials to obtain the slopes and offsets of Figs. 4(a)–4(c). From this, one can then infer the k_0^{Me}, k_1^{Me}, and $\tilde{\gamma}_\infty$ parameters (and therewith $\tilde{\gamma}^{Me}$) for any other material or surface orientation based on the calculation of the adsorption energy of a single water molecule.

C. Effect of the lattice

The careful eye notices that our fit to the data in Fig. 3(b) is not perfect, but the data points rather oscillate around an average trend captured by the fit function. To further investigate this behavior and demonstrate the overall convergence of our setup, we performed a more detailed analysis for Pt, Au, and Pb. Only cavities centered in the adsorbed water layer were considered; however, the studied size range was increased up to 9.5 Å and the MD runtime was significantly extended to 2.5 ns. Free energy differences F_{cav}^* are computed between all sizes and a reference calculation without a cavity. Figure 5(a) displays the area-normalized quantity $F_{cav}^*/\pi r_{cav}^2$ from this and the previous set of calculations (cf. Fig. S1 of the supplementary material), demonstrating the overall convergence and revealing that the oscillations are neither an artifact of our free energy calculation nor the fitting procedure. Renormalizing the cavity size to the substrates' nearest-neighbor distances results in the alignment of the oscillations across all substrates [Fig. 5(b)]. The oscillations thus likely arise from the preference of water to adsorb at specific sites, and an increase in the (normalized) cavity radius leads to the sequential exclusion of different sets of adsorption sites and thus oscillating cavity formation energies. As an example, the blocking of top sites demands less energy for the present force field (see Table S4 of the supplementary material), leading to a shallow slope between $1.7 \leq d_{NN} \leq 2.0$, while the blocking of fcc/hcp sites between $1.1 \leq d_{NN} \leq 1.6$ results in a steep slope. This hypothesis is supported by the observed shifted oscillations, when placing the cavities at a

different lateral position (see Fig. S3 of the supplementary material). Although these deviations of ~0.1 eV from the average trend are relevant for small cavities, their magnitude becomes increasingly negligible compared to the overall free energy cost for larger cavities. Similarly, the impact on the differences between different substrate materials is only minor, which justifies our oscillation-free fit with a smooth, low-order polynomial, as above.

Nonetheless, the choice of the force field plays a crucial role in this regard. Static[49,50] and dynamic[51,52] first-principle calculations have shown that water preferably adsorbs on the top site of the investigated metal surfaces. However, the employed force field predicts adsorption on the threefold coordinated hcp and fcc sites (cf. Table S4 of the supplementary material). Therefore, the oscillations in Fig. S3(B) of the supplementary material should have a maximum when we replace water from the favorable top site and a minimum for the less favorable hcp/fcc sites for more realistic models. The amplitude depends likely on the energetic difference between the adsorption sites.

Finally, the interface tension $\tilde{\gamma}^{Me}$ of the metal–water interface and the convergence tendency (k_0^{Me}, k_1^{Me}) against this value might be affected by a different calculation method as well. However, the comparison with the existing theoretical and experimental benchmarks in Sec. IV underlines that our results are within a reasonable range.

IV. SUMMARY AND CONCLUSION

Our results demonstrate that cavity formation at solid–liquid interfaces is strongly substrate-dependent and that the observed trends are fully consistent with the idea of competitive adsorption. In general, cavitation energies F_{cav} increase with cavity size and substrate reactivity. Both dependencies can be fully rationalized based on a simple geometric Gibbs model that explains F_{cav} via the free energy cost of introduced interfaces—namely the cavity–solvent and cavity–solid interfaces. The creation of the cavity–solid interface is

associated with removing interfacial solvent from a given surface contact area, and, as a result, its energy cost correlates with the adsorption strength of individual solvent molecules. Using expressions from SPT, the parameters of the Gibbs model exhibit even a simple, intelligible linear correlation with this adsorption strength. On the one hand, this opens an avenue for the simple parametrization of a general interface-aware cavitation model that could replace the existing bulk cavitation models in common implicit solvation approaches. On the other hand, it suggests that the present insight gained specifically for water is transferable to other solvents as well.

One shortcoming of the current setup is the omission of polarization effects. Therefore, we computed the cavity formation energy on Au(111) with a polarizable force field,[53] which is based on the same framework and adds a core–shell description for the metal. The results agree well with the ones obtained from the non-polarizable force field (cf. Fig. S6 of the supplementary material), which is not surprising since the interface tensions of both models are similar ($\tilde{\gamma}^{Au} = 0.30$ J m^{-2} vs $\tilde{\gamma}^{Au}_{pol} = 0.32$ J m^{-2}).[28,53]

Apart from generating leads to improved solvation models, the here identified trends also provide important insights into the general relevance and effects of competitive adsorption. The observed material- and size-dependence of the effective interface energies leads to cavity formation energies for small adsorbates ($r_{cav} \approx 3$ Å) that are, on the one hand, significantly smaller than that estimated from the macroscopic interface tensions [e.g., by a factor of 2 for Pt(111)] and that, on the other hand, exhibit a smaller-than-expected spread between the different substrates, which makes the missing account in existing implicit solvation methods less dramatic.[54] However, the account of competitive adsorption is crucial for understanding the stability of large adsorbates.[26,55–57] This is, for example, already the case for phenol[21,22,26,58,59] ($r_{cav} \approx 4.35$ Å), for which the adsorption energy on Pt(111) in an aqueous environment is smaller by 1.6 eV than in gas phase.[26] While schemes that include explicit solvation through QM/MM setups[21] or the three-dimensional reference interaction site model (3D-RISM)[58] predict a comparable reduction as the experiment, current implicit solvation models leave the adsorption energy in solvent essentially unchanged.[21,22,60,61] However, including cavitation free energy costs via geometric considerations already explains an additional energy cost of ~0.95 eV, as estimated from our model and similarly from the model of Akinola *et al.* (0.92 eV) when assuming a contact area of $A_{SC} \sim 60$ Å^2[26] and $\tilde{\gamma}^{Pt} = 16$ meV Å^{-2}. An according energy cost can be included in the non-electrostatic cavitation energy descriptions of implicit models by making these curvature- and substrate-dependent—a possible pathway for future improved implementations.

Another important aspect of competitive adsorption in solvent is the reduction in reactivity differences between different substrates or adsorption sites. This arises from the fact that reactive sites are typically more reactive toward not only a given adsorbate but also the solvent molecules, thus leading to higher cavitation costs at more reactive sites and thus to differences in adsorption energies in solvent that are smaller than in vacuum. Trends such as prevalent volcano plots in surface catalysis may, therefore, be distorted when computed in vacuum, with the amount of distortion depending on overall reactivity, e.g., the coordination of considered adsorption site.[60,62] As an example, reactive edge and kink sites that are characterized as too strongly binding or poisoned in vacuum

calculations might as well exhibit suitable reactivity upon immersion in solvent.

SUPPLEMENTARY MATERIAL

The supplementary file contains the following:

- Table S1: The lattice constant and number of water molecules for each investigated system.
- Table S2: The effective interface tensions for all investigated sizes and interfaces.
- Table S3: The polynomial coefficients to fit the size-dependent interface tensions.
- Table S4: Adsorption energies of a single water molecule on each metal surface for the different adsorption sites.
- Figure S1: Free energy profiles of all metal–water interfaces for all investigated sizes.
- Figure S2: Free energy profiles of all metal–water interfaces for all investigated sizes, including a repulsive metal–cavity interaction.
- Figure S3: Comparison between the cavity formation free energy at the Pt(111)/water interface for the adsorption on the top and hcp site.
- Figure S4: Oxygen density profile along the surface normal and areal density of adsorbed water molecules on the studied metal substrates as a function of adsorption energy.
- Figure S5: Weeks–Chandler–Andersen potentials for the seven investigated cavity sizes.
- Figure S6: Comparison of cavity formation energies at the Au(111)/water interface as obtained from the non-polarizable and polarizable force fields.
- Figure S7: Comparison of cavity formation energies at the Pt(111)/water interface as obtained for two different cavity geometries (one sphere and a chain of three spheres).

AUTHOR DECLARATIONS

Conflict of Interest

The authors have no conflicts to disclose.

Author Contributions

Thorben Eggert: Conceptualization (equal); Data curation (lead); Formal analysis (lead); Investigation (lead); Methodology (equal); Visualization (lead); Writing – original draft (equal); Writing – review & editing (equal). **Nicolas G. Hörmann**: Conceptualization (equal); Methodology (equal); Supervision (equal); Writing – original draft (equal); Writing – review & editing (equal). **Karsten Reuter**: Conceptualization (equal); Funding acquisition (equal);

Supervision (equal); Writing – original draft (equal); Writing – review & editing (equal).

DATA AVAILABILITY

The results of the interface tensions for all investigated systems and the obtained coefficients for Eq. (5) are tabulated in the supplementary file. In addition, it contains information about the setup (lattice constant and number of water molecules) for each system.

The data for the energy profiles (resulting from the free energy integration, the initially fitted Gibbs model, and the model using the observed linear relations) are uploaded to https://doi.org/10.17617/3.WERJXN, together with an exemplary input script.

APPENDIX: EFFECTIVE SURFACE TENSION OF WATER

The effective surface tension for bulk water $\gamma_{LC}(r_{cav})$ was fitted to the free energy profile in the range between $z_{top} + r_{cut} + 5$ Å and $z_{top} + r_{cut} + 10$ Å. This ensures that the cavity is always fully surrounded by bulk water, and therefore, the cavity formation energy is constant. After fixing $\gamma_{LC}(r_{cav})$, the effective interface tensions $\tilde{\gamma}^{Me}(r_{cav})$ and z_{offset}^{Me} were fitted through Eq. (4) and shifting of the free energy profile. The macroscopic surface tension of liquid water γ_{LV} was calculated from the ensemble-averaged pressure tensor[63] via

$$\gamma_{LV} = \frac{L_z}{2}\left\langle p_{zz} - \frac{1}{2}(p_{xx} + p_{yy})\right\rangle. \tag{A1}$$

For this purpose, we created a cube of $(40 \text{ Å})^3$ filled with 2140 water molecules. After adding 30 Å of vacuum along the z direction on both sides and running an NVT-MD for 10 ns, we determined a surface tension of 48.2 mJ m^{-2}.

REFERENCES

[1] O. Björneholm, M. H. Hansen, A. Hodgson, L.-M. Liu, D. T. Limmer, A. Michaelides, P. Pedevilla, J. Rossmeisl, H. Shen, G. Tocci, E. Tyrode, M.-M. Walz, J. Werner, and H. Bluhm, "Water at interfaces," Chem. Rev. **116**, 7698–7726 (2016).

[2] V. Molinero and E. B. Moore, "Water modeled as an intermediate element between carbon and silicon," J. Phys. Chem. B **113**, 4008–4016 (2009).

[3] K. Forster-Tonigold and A. Groß, "Dispersion corrected RPBE studies of liquid water," J. Chem. Phys. **141**, 064501 (2014).

[4] M. J. Gillan, D. Alfè, and A. Michaelides, "Perspective: How good is DFT for water?," J. Chem. Phys. **144**, 130901 (2016).

[5] J. Tomasi and M. Persico, "Molecular interactions in solution: An overview of methods based on continuous distributions of the solvent," Chem. Rev. **94**, 2027–2094 (1994).

[6] J. Tomasi, B. Mennucci, and R. Cammi, "Quantum mechanical continuum solvation models," Chem. Rev. **105**, 2999–3094 (2005).

[7] D. Chandler, "Interfaces and the driving force of hydrophobic assembly," Nature **437**, 640–647 (2005).

[8] S. Höfinger and F. Zerbetto, "Simple models for hydrophobic hydration," Chem. Soc. Rev. **34**, 1012 (2005).

[9] F. V. Grigor'ev, M. V. Bazilevskii, S. N. Zhabin, A. N. Romanov, and V. B. Sulimov, "Calculations of the Gibbs energy of formation of cavities in water," Russ. J. Phys. Chem. **82**, 517–525 (2008).

[10] H. Reiss, H. L. Frisch, and J. L. Lebowitz, "Statistical mechanics of rigid spheres," J. Chem. Phys. **31**, 369–380 (1959).

[11] R. A. Pierotti, "A scaled particle theory of aqueous and nonaqueous solutions," Chem. Rev. **76**, 717–726 (1976).

[12] A. Pohorille and L. R. Pratt, "Cavities in molecular liquids and the theory of hydrophobic solubilities," J. Am. Chem. Soc. **112**, 5066–5074 (1990).

[13] G. Hummer, S. Garde, A. E. García, A. Pohorille, and L. R. Pratt, "An information theory model of hydrophobic interactions," Proc. Natl. Acad. Sci. U. S. A. **93**, 8951–8955 (1996).

[14] F. M. Floris, M. Selmi, A. Tani, and J. Tomasi, "Free energy and entropy for inserting cavities in water: Comparison of Monte Carlo simulation and scaled particle theory results," J. Chem. Phys. **107**, 6353–6365 (1997).

[15] I. Sedov and T. Magsumov, "The Gibbs free energy of cavity formation in a diverse set of solvents," J. Chem. Phys. **153**, 134501 (2020).

[16] D. A. Scherlis, J.-L. Fattebert, F. Gygi, M. Cococcioni, and N. Marzari, "A unified electrostatic and cavitation model for first-principles molecular dynamics in solution," J. Chem. Phys. **124**, 074103 (2006).

[17] O. Andreussi, I. Dabo, and N. Marzari, "Revised self-consistent continuum solvation in electronic-structure calculations," J. Chem. Phys. **136**, 064102 (2012).

[18] A. V. Marenich, C. J. Cramer, and D. G. Truhlar, "Generalized Born solvation model SM12," J. Chem. Theory Comput. **9**, 609–620 (2013).

[19] J. Zhang, H. Zhang, T. Wu, Q. Wang, and D. van der Spoel, "Comparison of implicit and explicit solvent models for the calculation of solvation free energy in organic solvents," J. Chem. Theory Comput. **13**, 1034–1043 (2017).

[20] H. H. Heenen, J. A. Gauthier, H. H. Kristoffersen, T. Ludwig, and K. Chan, "Solvation at metal/water interfaces: An *ab initio* molecular dynamics benchmark of common computational approaches," J. Chem. Phys. **152**, 144703 (2020).

[21] P. Clabaut, B. Schweitzer, A. W. Götz, C. Michel, and S. N. Steinmann, "Solvation free energies and adsorption energies at the metal/water interface from hybrid quantum-mechanical/molecular mechanics simulations," J. Chem. Theory Comput. **16**, 6539–6549 (2020).

[22] G. Bramley, M.-T. Nguyen, V.-A. Glezakou, R. Rousseau, and C.-K. Skylaris, "Reconciling work functions and adsorption enthalpies for implicit solvent models: A Pt (111)/water interface case study," J. Chem. Theory Comput. **16**, 2703–2715 (2020).

[23] S. N. Steinmann, P. Sautet, and C. Michel, "Solvation free energies for periodic surfaces: Comparison of implicit and explicit solvation models," Phys. Chem. Chem. Phys. **18**, 31850–31861 (2016).

[24] S. Ringe, N. G. Hörmann, H. Oberhofer, and K. Reuter, "Implicit solvation methods for catalysis at electrified interfaces," Chem. Rev. **122**, 10777–10820 (2022).

[25] H. H. Kristoffersen, J.-E. Shea, and H. Metiu, "Catechol and HCl adsorption on TiO$_2$(110) in vacuum and at the water–TiO$_2$ interface," J. Phys. Chem. Lett. **6**, 2277–2281 (2015).

[26] J. Akinola, C. T. Campbell, and N. Singh, "Effects of solvents on adsorption energies: A general bond-additivity model," J. Phys. Chem. C **125**, 24371–24380 (2021).

[27] P. Dauber-Osguthorpe, V. A. Roberts, D. J. Osguthorpe, J. Wolff, M. Genest, and A. T. Hagler, "Structure and energetics of ligand binding to proteins: *Escherichia coli* dihydrofolate reductase-trimethoprim, a drug-receptor system," Proteins: Struct., Funct., Bioinf. **4**, 31–47 (1988).

[28] H. Heinz, R. A. Vaia, B. L. Farmer, and R. R. Naik, "Accurate simulation of surfaces and interfaces of face-centered cubic metals using 12–6 and 9–6 Lennard-Jones potentials," J. Phys. Chem. C **112**, 17281–17290 (2008).

[29] A. Hjorth Larsen, J. Jørgen Mortensen, J. Blomqvist, I. E. Castelli, R. Christensen, M. Dułak, J. Friis, M. N. Groves, B. Hammer, C. Hargus, E. D. Hermes, P. C. Jennings, P. Bjerre Jensen, J. Kermode, J. R. Kitchin, E. Leonhard Kolsbjerg, J. Kubal, K. Kaasbjerg, S. Lysgaard, J. Bergmann Maronsson, T. Maxson, T. Olsen, L. Pastewka, A. Peterson, C. Rostgaard, J. Schiøtz, O. Schütt, M. Strange, K. S. Thygesen, T. Vegge, L. Vilhelmsen, M. Walter, Z. Zeng, and K. W. Jacobsen, "The atomic simulation environment—A Python library for working with atoms," J. Phys.: Condens. Matter **29**, 273002 (2017).

[30] L. Martínez, R. Andrade, E. G. Birgin, and J. M. Martínez, "PACKMOL: A package for building initial configurations for molecular dynamics simulations," J. Comput. Chem. **30**, 2157–2164 (2009).

[31] A. P. Thompson, H. M. Aktulga, R. Berger, D. S. Bolintineanu, W. M. Brown, P. S. Crozier, P. J. in 't Veld, A. Kohlmeyer, S. G. Moore, T. D. Nguyen, R. Shan, M. J. Stevens, J. Tranchida, C. Trott, S. J. Plimpton, and S. J. Plimpton,

"LAMMPS—A flexible simulation tool for particle-based materials modeling at the atomic, meso, and continuum scales," Comput. Phys. Commun. **271**, 108171 (2022).

[32] D. M. Heyes and H. Okumura, "Some physical properties of the Weeks–Chandler–Andersen fluid," Mol. Simul. **32**, 45–50 (2006).

[33] D. Ben-Amotz and G. Stell, "Reformulation of Weeks–Chandler–Andersen perturbation theory directly in terms of a hard-sphere reference system," J. Phys. Chem. B **108**, 6877–6882 (2004).

[34] M. R. Shirts and J. D. Chodera, "Statistically optimal analysis of samples from multiple equilibrium states," J. Chem. Phys. **129**, 124105 (2008).

[35] D. T. Limmer, A. P. Willard, P. Madden, and D. Chandler, "Hydration of metal surfaces can be dynamically heterogeneous and hydrophobic," Proc. Natl. Acad. Sci. U. S. A. **110**, 4200–4205 (2013).

[36] A. Serva, M. Salanne, M. Havenith, and S. Pezzotti, "Size dependence of hydrophobic hydration at electrified gold/water interfaces," Proc. Natl. Acad. Sci. U. S. A. **118**, e2023867118 (2021).

[37] R. Godawat, S. N. Jamadagni, and S. Garde, "Characterizing hydrophobicity of interfaces by using cavity formation, solute binding, and water correlations," Proc. Natl. Acad. Sci. U. S. A. **106**, 15119–15124 (2009).

[38] O. Andreussi, N. G. Hörmann, F. Nattino, G. Fisicaro, S. Goedecker, and N. Marzari, "Solvent-aware interfaces in continuum solvation," J. Chem. Theory Comput. **15**, 1996–2009 (2019).

[39] J. W. Gibbs, *Collected Works* (Yale University Press, New Haven, 1948), Vol. I, pp. 219–237.

[40] G. G. Láng, "Basic interfacial thermodynamics and related mathematical background," ChemTexts **1**, 16 (2015).

[41] A. Serva, M. Havenith, and S. Pezzotti, "The role of hydrophobic hydration in the free energy of chemical reactions at the gold/water interface: Size and position effects," J. Chem. Phys. **155**, 204706 (2021).

[42] J. Dzubiella, J. M. J. Swanson, and J. A. McCammon, "Coupling nonpolar and polar solvation free energies in implicit solvent models," J. Chem. Phys. **124**, 084905 (2006).

[43] J. A. Wagoner and N. A. Baker, "Assessing implicit models for nonpolar mean solvation forces: The importance of dispersion and volume terms," Proc. Natl. Acad. Sci. U. S. A. **103**, 8331–8336 (2006).

[44] H. J. C. Berendsen, J. P. M. Postma, W. F. van Gunsteren, and J. Hermans, "Interaction models for water in relation to protein hydration," in *Intermolecular Forces: Proceedings of the Fourteenth Jerusalem Symposium on Quantum Chemistry and Biochemistry Held in Jerusalem, Israel, April 13–16, 1981*, edited by B. Pullman (Springer, Netherlands, Dordrecht, 1981), pp. 331–342.

[45] S. P. Kadaoluwa Pathirannahalage, N. Meftahi, A. Elbourne, A. C. G. Weiss, C. F. McConville, A. Padua, D. A. Winkler, M. Costa Gomes, T. L. Greaves, T. C. Le, Q. A. Besford, and A. J. Christofferson, "Systematic comparison of the structural and dynamic properties of commonly used water models for molecular dynamics simulations," J. Chem. Inf. Model. **61**, 4521–4536 (2021).

[46] W. L. Jorgensen, J. Chandrasekhar, J. D. Madura, R. W. Impey, and M. L. Klein, "Comparison of simple potential functions for simulating liquid water," J. Chem. Phys. **79**, 926–935 (1983).

[47] R. C. Tolman, "The effect of droplet size on surface tension," J. Chem. Phys. **17**, 333–337 (1949).

[48] S. Gim, K. J. Cho, H.-K. Lim, and H. Kim, "Structure, dynamics, and wettability of water at metal interfaces," Sci. Rep. **9**, 14805 (2019).

[49] A. Michaelides, "Density functional theory simulations of water–metal interfaces: Waltzing waters, a novel 2D ice phase, and more," Appl. Phys. A **85**, 415–425 (2006).

[50] J. Carrasco, A. Michaelides, and M. Scheffler, "Insight from first principles into the nature of the bonding between water molecules and 4d metal surfaces," J. Chem. Phys. **130**, 184707 (2009).

[51] S. Schnur and A. Groß, "Properties of metal–water interfaces studied from first principles," New J. Phys. **11**, 125003 (2009).

[52] S. Sakong and A. Groß, "Water structures on a Pt(111) electrode from *ab initio* molecular dynamic simulations for a variety of electrochemical conditions," Phys. Chem. Chem. Phys. **22**, 10431–10437 (2020).

[53] I. L. Geada, H. Ramezani-Dakhel, T. Jamil, M. Sulpizi, and H. Heinz, "Insight into induced charges at metal surfaces and biointerfaces using a polarizable Lennard–Jones potential," Nat. Commun. **9**, 716 (2018).

[54] J. Park and L. T. Roling, "Elucidating energy scaling between atomic and molecular adsorbates in the presence of solvent," AIChE J. **66**, e17036 (2020).

[55] J. O. Bockris and K. T. Jeng, "In-situ studies of adsorption of organic compounds on platinum electrodes," J. Electroanal. Chem. **330**, 541–581 (1992).

[56] N. Singh and C. T. Campbell, "A simple bond-additivity model explains large decreases in heats of adsorption in solvents versus gas phase: A case study with phenol on Pt(111) in water," ACS Catal. **9**, 8116–8127 (2019).

[57] J. R. Rumptz and C. T. Campbell, "Adhesion energies of solvent films to Pt(111) and Ni(111) surfaces by adsorption calorimetry," ACS Catal. **9**, 11819–11825 (2019).

[58] A. Takamatsu, M. Higashi, and H. Sato, "Free energy and solvation structure analysis for adsorption of aromatic molecules at Pt(111)/water interface by 3D-RISM theory," Chem. Lett. **51**, 791–795 (2022).

[59] M. Zare, M. S. Saleheen, N. Singh, M. J. Uline, M. Faheem, and A. Heyden, "Liquid-phase effects on adsorption processes in heterogeneous catalysis," JACS Au **2**, 2119–2134 (2022).

[60] J. Akinola, I. Barth, B. R. Goldsmith, and N. Singh, "Adsorption energies of oxygenated aromatics and organics on rhodium and platinum in aqueous phase," ACS Catal. **10**, 4929–4941 (2020).

[61] G. A. Bramley, M.-T. Nguyen, V.-A. Glezakou, R. Rousseau, and C.-K. Skylaris, "Understanding adsorption of organics on Pt(111) in the aqueous phase: Insights from DFT based implicit solvent and statistical thermodynamics models," J. Chem. Theory Comput. **18**, 1849–1861 (2022).

[62] S. D. Beinlich, N. G. Hörmann, and K. Reuter, "Field effects at protruding defect sites in electrocatalysis at metal electrodes?," ACS Catal. **12**, 6143–6148 (2022).

[63] D. Bhatt, J. Newman, and C. J. Radke, "Molecular dynamics simulations of surface tensions of aqueous electrolytic solutions," J. Phys. Chem. B **108**, 9077–9084 (2004).

09 January 2024 09:34:10